Nanoscale

ROYAL SOCIETY OF CHEMISTRY

PAPER

View Article Online
View Journal | View Issue

Cite this: *Nanoscale*, 2024, **16**, 19306

Engineering multi-component 3DOM $FeVCrO_x$ catalysts with high oxygen mobility for the oxidative dehydrogenation of 1-butene with CO_2†

Xiaoshuai Gao,[a,b] Weigao Han,*[b] Fang Dong,[b] Xiaosheng Huang,[b] Zhicheng Tang *[b] and Qiuye Li *[a]

Received 20th July 2024,
Accepted 16th September 2024

DOI: 10.1039/d4nr03011g

rsc.li/nanoscale

Oxidative dehydrogenation (ODH) of 1-butene with CO_2 to 1,3-butadiene (BD) *via* Fe-based catalysts is a promising strategy, and the mobility of lattice oxygen plays a key role in the catalytic reaction. However, the catalytic activity of Fe-based catalysts is limited by the poor lattice oxygen mobility. To improve the mobility of lattice oxygen and optimize the ODH reaction, a series of 3DOM Fe-based catalysts ($FeVAlO_x$, $FeCrAlO_x$, and $FeVCrAlO_x$) were prepared by PMMA template method. Among these samples, the multi-component $FeVCrAlO_x$ samples showed the best catalytic activity, and the 1-butene conversion of the multi-component catalyst could reach 88.3%, the BD yield could reach 27.5%. Further study found that the introduction of multi-component elements (V and Cr) not only promoted the formation of the γ-Fe_2O_3 phase but also formed more active components (V^{5+} and Cr^{6+}). More importantly, the lattice oxygen mobility was also significantly improved. In addition, the reaction in the presence of water conditions was studied by activity tests and *in situ* DRIFTS tests. The results show that CO_2 was present in the form of HCO_3^-. The utilization of CO_2 was improved and the reaction path was changed.

1. Introduction

1,3-Butadiene (BD) is a critical building block in the petrochemical industry, and it is used in synthetic rubber, resins, and fine chemicals. Due to the rapid growth of the industry, BD has seen continuous and rapid growth in demand.[1–3] Traditionally, it is produced by separating C_4 fractions and oxidative dehydrogenation (ODH) procedures.[4] Due to the low yield and production of CO_2, neither of them is an effective strategy for preparing the BD. Therefore, the development of new processes has become a trend. It is worth noting that CO_2-ODH (eqn (1)) is an environmentally friendly and sustainable approach.[5] It not only effectively utilizes greenhouse gases, but also produces high-value products like BD. And the weak oxidation of CO_2 is helpful in avoiding over-oxidation of the product, reducing coke formation, and improving the stability of the catalyst.[6,7] However, there are still other challenges: the breakage energy of C=O bonds in CO_2 is 750 kJ mol^{-1}, which makes it difficult to utilize CO_2.[8] The coke formation also reduces the stability of the catalyst.[9,10] So, we designed a catalyst and aimed at solving these problems.

$$CH_2{=}CH\text{-}CH_2CH_3 + CO_2 \rightarrow CH_2{=}CH\text{-}CH{=}CH_2 + CO + H_2O \quad (1)$$

Due to the high catalytic activity, Fe-based catalysts have been widely studied.[11–13] In the O_2-ODH of butene, Yang *et al.*[14] found that γ-Fe_2O_3 showed better activity than α-Fe_2O_3. In Lee's paper,[15] a series of $M^{II}Fe_2O_4$ catalysts (M^{II} = Zn, Mg, Mn, Ni, Co, Cu) based on iron catalysts were prepared. The result showed that single-element doping changed the surface acidity of the catalysts. Among them, $ZnFe_2O_4$ with more surface acidity had a higher BD yield. In the study of Toledo *et al.*[16] Al^{3+} was introduced into $ZnFeO_4$, and the results showed that the Fe^{3+} in the octahedral sites was replaced. As a result, the lattice parameters increased, and the symmetry of electron distribution pairs around Fe^{3+} decreased. Then the charge transfer between Fe^{3+} and lattice oxygen was promoted. In the chemical looping oxidative dehydrogenation of ethane, Hye Jeong *et al.* prepared Ce-doped $FeTiO_x$ ($FeCeTiO_x$) by one-pot method.[17] The introduction of Ce enhanced the lattice oxygen mobility and the catalytic performance of $FeCeTiO_x$ was improved. The $FeCeTiO_x$ also revealed excellent cyclic stability with a stable C_2H_4 formation rate and C_2H_4 selectivity

[a]*National & Local Joint Engineering Research Center for Applied Technology of Hybrid Nanomaterials, Henan University, Kaifeng 475004, China. E-mail: qiuyeli@henu.edu.cn*
[b]*National Engineering Research Center for Fine Petrochemical Intermediates, State Key Laboratory for Oxo Synthesis and Selective Oxidation, Lanzhou Institute of Chemical Physics, Chinese Academy of Sciences, Lanzhou 730000, China. E-mail: wghan17@licp.cas.cn, tangzhicheng@licp.cas.cn*

†Electronic supplementary information (ESI) available. See DOI: https://doi.org/10.1039/d4nr03011g

of 84.1%. In the CO_2-ODH of propane, Zhang *et al.* introduced Fe into impregnated V-Al_2O_3, and the dual-sites catalyst (FeV/Al_2O_3) including Fe and V was constructed.[18] V is the main active site for C_3H_8 dehydrogenation while Fe is responsible for the CO_2 dissociation, replenishing lattice oxygen. And the catalyst achieved a C_3H_8 conversion at ~43%, C_3H_6 selectivity exceeded 80%. It could be found that the introduction of multiple elements could improve the performance of the catalyst. In dehydrogenation reactions, V and Cr are often used as active elements. Moreover, the radius of V, Cr and Fe are similar, and the V and Cr have more valence states. This allows V and Cr to replace iron elements in the lattice, and it will lead to a change in the crystal structure and an increase in lattice defects. Therefore, by introducing V, Cr in Fe-based catalysts, the oxygen mobility and catalytic activity are expected to be improved.[19–22]

Water is considered to be a frequent influence in the reaction process. Several studies have shown that the introduction of water might lead to the generation of side reactions and the reduction of product selectivity as well as the shortening of catalyst life.[23] In the study of the complete oxidation of methane, Zhao *et al.*[24] found that the introduction of water led to the deactivation of the catalyst. The reasons were suggested: on the one hand, the competitive adsorption between water and CH_4 at the surface-active sites caused the reversible deactivation. On the other hand, water vapor caused Pd agglomeration on the surface of the catalyst, which led to irreversible deactivation. However, the results of the presence of water were opposite in other studies.[25] In the study of non-oxidative propane dehydrogenation, Long *et al.*[26] found that water pretreatment promoted the reduction rearrangement of Co catalytic sites. Compared with the untreated catalyst, the reaction activity was increased by 7 times. The role of water in the O_2-ODH of 1-butene was studied by Zeng *et al.*[11] Both experimental and theoretical studies showed that in the presence of water, the surface-unstable O was converted into a more thermally stable hydroxyl group. The hydroxyl group was considered to be the active site of C–H bond cleavage, which is beneficial to the reaction. It could be found that water plays different roles in different reactions. Moreover, the influence of water in the 1-butene CO_2-ODH reaction is still open, and the reaction mechanism involving water remains elusive. In this paper, the influence on the catalytic activity under different volume fractions was studied, and the *in situ* DRIFTS was used to study the reaction path in the presence of water, the possible pathway was suggested.

The paper aimed to investigate the relationship between the introduction of elements and the lattice oxygen mobility. The effect of water on the reactivity was also investigated and the possible reaction pathway was suggested. Hence, a series of multi-component catalysts were prepared for activity testing. Detailed characterizations were also carried out to study the influence of elemental introduction on the catalyst properties. The XPS was used to analyze the changes in lattice oxygen and the *in situ* DRIFTS tests demonstrated the role of water in the reaction. In addition, TPR, TPD, TPO, SEM, TEM, XRD, Raman, and BET were used to investigate the effect of the element introduction on the performance and morphology structure. The results showed that the multi-component (V, Cr) introduction promoted lattice oxygen mobility, and water facilitated the whole reaction by changing the reaction path. Meanwhile, it was found that the introduction of V played an important role in reducing the coke formation, the reduction ability of the catalyst was improved by the introduction of Cr. In this work, the lattice oxygen mobility was improved by the introduction of multi-component, and the CO_2-ODH was optimized by the positive assistance of water. We hope this study could provide new ideas for efficient CO_2-ODH.

2. Experimental

2.1. Samples preparation

2.1.1. Preparation of highly ordered polymethyl methacrylate (PMMA) microspheres. PMMA was prepared in a nitrogen-protected environment.[27,28] First, 240 ml of deionized water was added to a three-necked flask and heated to 80 °C. Then 120 ml of MMA was added and mixed thoroughly for 20 minutes. After that, the preheated 80 °C initiator solution (6 g of potassium persulfate dissolved in 40 ml of deionized water) was added to the three-necked flask. Following that, the mixed solution was reacted at 80 °C for 2 h. The solution was filtered through a microfiltration membrane and the filtrate was collected. Finally, the filtrate was centrifuged at 3000 rpm for 10 hours and dried at 40 °C for 12 hours to obtain a three-dimensionally ordered PMMA microsphere template.

2.1.2. Preparation of three-dimensional ordered macro–mesoporous Al_2O_3 samples. The soft and hard templates were used to create a three-dimensional ordered macro–mesoporous structure. First, a solution of mesoporous Al precursor was prepared. 20 ml of ethanol was mixed with 1 g of P123, 2.04 g of aluminum isopropoxide, and 1.6 ml of HNO_3. After that, the solution was stirred for 5 hours to completely dissolve the solute. Then PMMA was completely impregnated in the precursor solution. Following that, the impregnated samples were dried at 40 °C for 24 hours. Finally, the dried samples were calcined in a tube furnace for 3 hours under the air atmosphere. The heating rate was 1 °C min^{-1} from room temperature to 650 °C. Finally, a three-dimensional ordered macro–mesoporous structure was obtained.

2.1.3. Preparation of three-dimensional ordered macro–mesoporous Fe-based samples. The preparation of the $FeVCrAlO_x$ catalyst is similar to the preparation method of the three-dimensional ordered macro–mesoporous Al_2O_3. By adding Fe, V, and Cr to the Al mesoporous precursor solution while keeping other conditions fixed, the $FeVCrO_x$ was obtained. Where the Al : Fe : V : Cr molar ratio is 10 : 5 : 1 : 1. Keeping the ratio of Fe and Al constant and changing the proportion of V and Cr a series of Fe-based catalysts $FeV_aCr_bAlO_x$ (a, b = 0, 1, 2, 3) were prepared. Finally, a series of three-dimensional ordered macro–mesoporous Fe-based catalysts were

obtained. Full details of the contents could be found in the Table S2.†

2.2. Activity measurement

The oxidative dehydrogenation of 1-butene with CO_2 was evaluated by a fixed-bed flow reactor operated in steady-state mode. A mixture of 0.2 g catalyst (40–60 mesh) and 0.4 g quartz sand (40–60 mesh) was placed in the reactor. Then the temperature was raised to 600 °C under the protection of nitrogen (60 ml min^{-1}). Subsequently, 60 ml min^{-1} of feed gas containing 1-butene/CO_2 (molar ratio 1 : 9) was fed. The weight hourly space velocity (WHSV) was 4.5 g $(g_{cat}\ h)^{-1}$. Finally, catalyst activity was tested in a stainless-steel reactor at 600 °C. During the reaction, the feed gas was controlled by a flow meter and the water was controlled by the Syringe Pump (TYD01-01). The products were analyzed by gas chromatograph equipped with two different detectors (TCD and FID), and the conversion and selectivity were determined by the external standard method. Calculation details were presented in ESI.†

3. Results and discussion

3.1. The synthesis mechanism of catalyst

As shown in Scheme 1, the three-dimensional ordered macro–mesoporous structure $FeVCrAlO_x$, $FeVAlO_x$, and $FeCrAlO_x$ catalysts were prepared by the soft and hard templates method. First, a solution of Al precursor with ordered mesopores was prepared. In order to improve the catalyst activity, the Fe element was confined into the Al_2O_3 framework. V and Cr were introduced to modify the crystal phase structure and release reactive oxygen species. The pore structure of the macro–mesoporous structure is aimed to provide a larger specific surface area and facilitate the diffusion of butene. The samples were used to study the synergistic effect of the introduction of multi-component on the catalytic performance.

3.2. Catalytic performance analysis

At 600 °C, the activity of the $FeVAlO_x$, $FeCrAlO_x$, and $FeVCrAlO_x$ catalysts was studied. Fig. 1 showed the stability for CO_2-ODH over samples. It could be found that the multi-component catalyst $FeVCrAlO_x$ exhibited a higher activity compared with the $FeVAlO_x$ and $FeCrAlO_x$ samples (Fig. 1a). The results showed that the conversion of 1-butene reached 88.3%, the BD yield reached 27.5%, the BD selectivity reached 31.2% and the CO_2 conversion reached 15.7%. However, the 1-butene conversion of $FeVAlO_x$ and $FeCrAlO_x$ was less than 60%, the BD yield was less than 17%, the BD selectivity was less than 30%, and the CO_2 conversion was less than 10%. This indicated that the introduction of V and Cr is beneficial to the improvement of

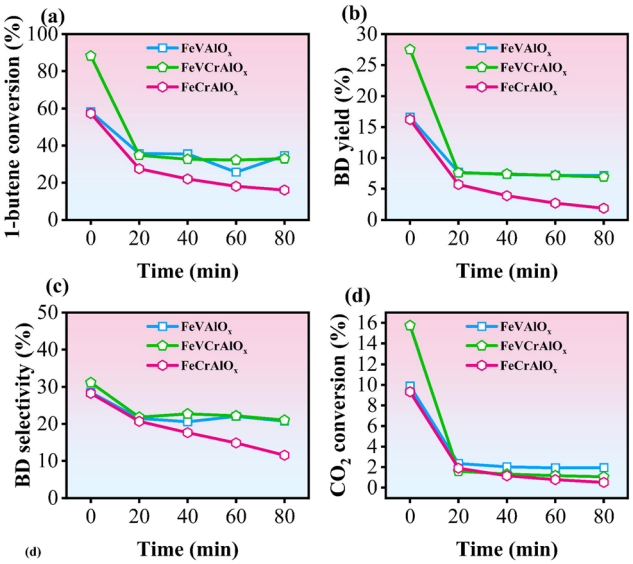

Fig. 1 The catalytic performance of $FeVAlO_x$, $FeCrAlO_x$, and $FeVCrAlO_x$ samples at 600 °C (a) 1-butene conversion, (b) BD yield, (c) BD selectivity, and (d) CO_2 conversion.

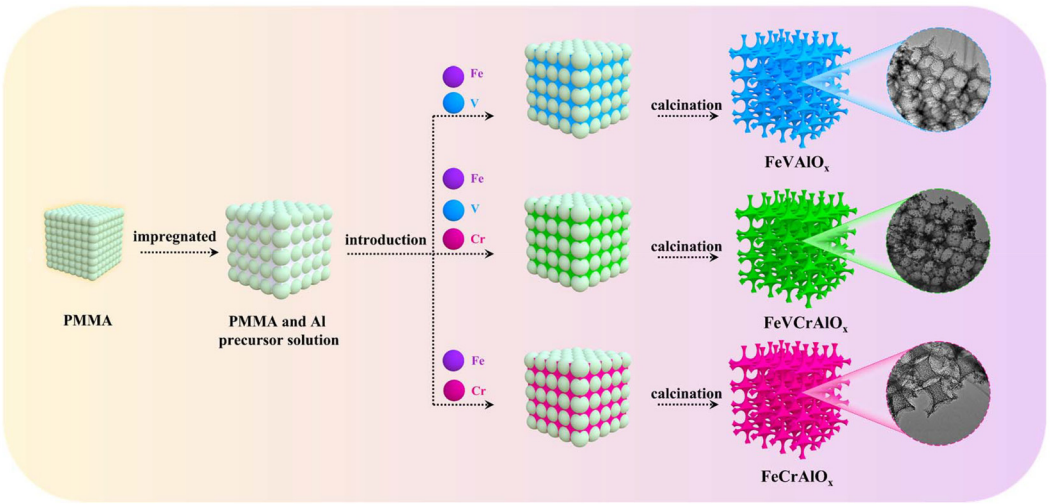

Scheme 1 Schematic showing the synthetic procedures.

activity and it was also further validated by the graph of $FeAlO_x$ catalyst activity as presented in Fig. S1.† Fig. S2† shows the product distribution of $FeVAlO_x$ $FeCrAlO_x$ $FeVCrAlO_x$ samples over time. It could be noticed that the $FeCrAlO_x$ yield decreased sharply, while the yield of the V-doped samples was relatively stable. This suggests that the introduction of V might be beneficial to improve the BD selectivity. In order to understand the role of V and Cr in catalytic activity, the activity of catalysts with different Cr and V contents was tested. As shown in Fig. 2, with the introduction of Cr, the activity of the catalysts increased first and then decreased. Finally, a maximum value appeared. It was found that the maximum CO_2 conversion of $FeVCr_2AlO_x$ reached 16.7% (Fig. 2d), it was higher than $FeVCrAlO_x$ (15.7%). This might indicate that the conversion of CO_2 was promoted by Cr. The introduction of V also showed the same trend (Fig. 3). The BD selectivity of FeV_2CrAlO_x reached 35% (Fig. 3d), which was also higher than $FeVCrAlO_x$ (31.2%). It might indicate that the introduction of V contributed to the selectivity of the BD. Therefore, the introduction of Cr was beneficial for the improvement of CO_2 conversion, while the introduction of V was beneficial for the improvement of selectivity. Based on the 1-butene conversion and BD yields, the catalysts exhibited the best activity at a 1 : 1 ratio of V and Cr (Fig. 1). Although $FeVCrAlO_x$ showed the best activity under the synergistic effect of V and Cr, it was quickly deactivated. Then, the conversion rate of the $FeVCrAlO_x$ catalyst at different temperatures was analyzed. As shown in Fig. S3,† no reaction occurred at 200 °C. When the temperature was increased to 300 °C, isomerization took place, but 1,3-butadiene was not produced. At 400 °C, dehydrogenation occurred, leading to the formation of 1,3-butadiene. With a further temperature increase to 500–600 °C, isomerization decreased, dehydrogenation increased, coking became significant, and cracking reactions occurred. This suggested that 1-butene first underwent isomerization to form 2-butene, which then converted to 1,3-butadiene. Coke formation likely occurred at higher temperatures, possibly because the products could not be desorbed in time. This will lead to the cracking and even coke formation. This ultimately caused rapid catalyst deactivation. The used catalyst was regenerated, and the results showed that the regeneration process partially recovered its activity but could not fully restore the catalyst to its initial performance levels (Fig. S4†). Subsequently, structural and morphological analyses were conducted to further investigate the issue of high activity but rapid deactivation of the catalyst.

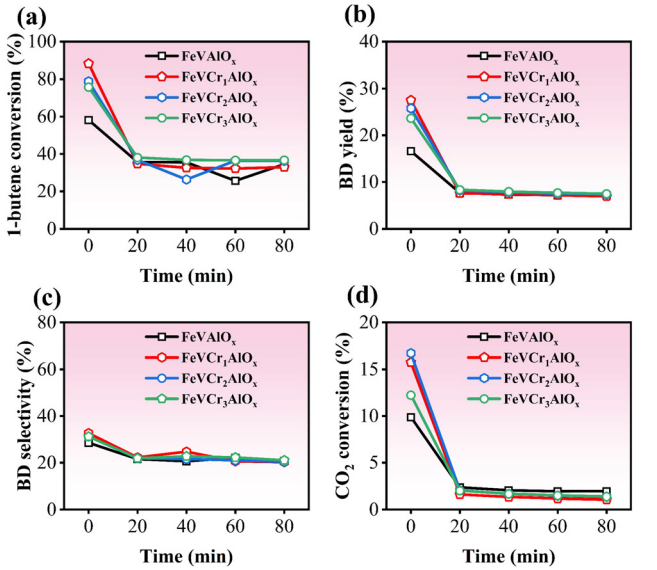

Fig. 2 Catalytic performance of samples with different Cr contents at 600 °C. (a) 1-Butene conversion, (b) BD yield, (c) BD selectivity, and (d) CO_2 conversion.

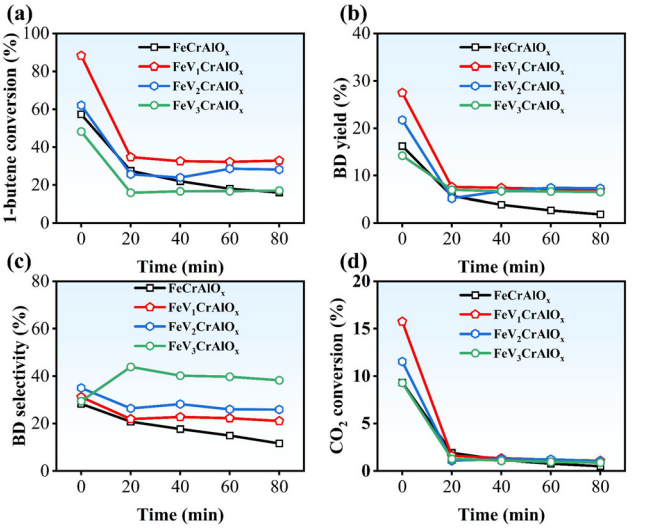

Fig. 3 Catalytic performance of samples with different V contents at 600 °C. (a) 1-Butene conversion, (b) BD yield, (c) BD selectivity, and (d) CO_2 conversion.

3.3. Structural and morphological analysis

The surface morphology of the samples was studied by SEM (Fig. 4). It could be found that $FeCrAlO_x$, $FeVAlO_x$, and $FeVCrAlO_x$ samples contained abundant ordered macroporous structures. When V and Cr were introduced, the unique macroporous structure of all samples was still maintained. The microstructure of the samples was studied by TEM (Fig. 5). Firstly, it could be found that all the samples maintained an ordered macroporous structure (Fig. 5a–h), which was consistent with the results of SEM. In addition, mesoporous structures were observed in $FeCrAlO_x$, $FeVAlO_x$, and $FeVCrAlO_x$ samples (Fig. 5i–l). Without the introduction of elements, Al_2O_3 had a highly ordered mesoporous structure. When Fe and Cr were introduced, the $FeCrAlO_x$ still maintained the ordered mesoporous (Fig. 5f and j). This indicated that the introduction of Cr would not destroy the three-dimensional ordered macro–mesoporous structure. However, after the introduction of V, it was found that the ordered mesoporous structure of $FeVAlO_x$ was destroyed (Fig. 5k). And a similar morphology was observed in $FeVCrAlO_x$

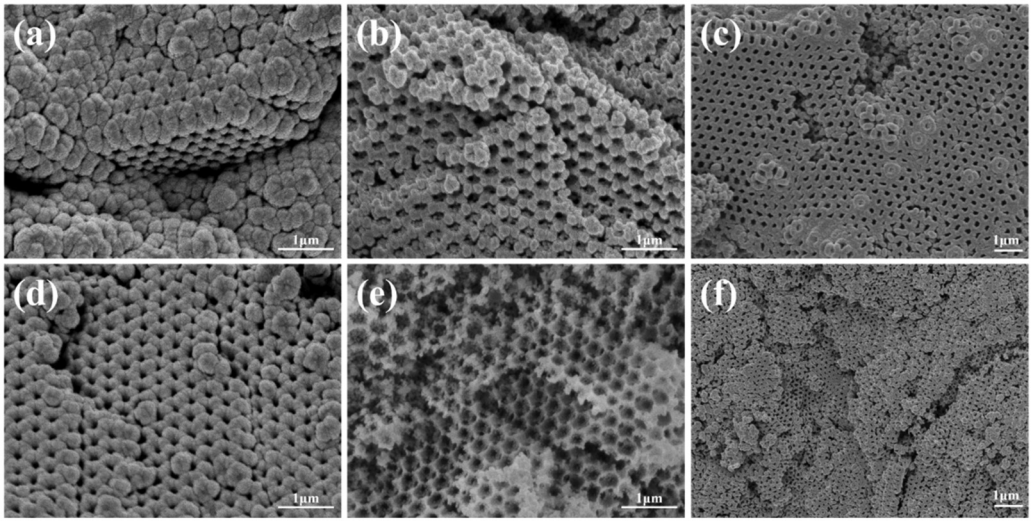

Fig. 4 SEM images of $FeCrAlO_x$ (a, d), $FeVAlO_x$ (b, e), and $FeVCrAlO_x$ (c, f).

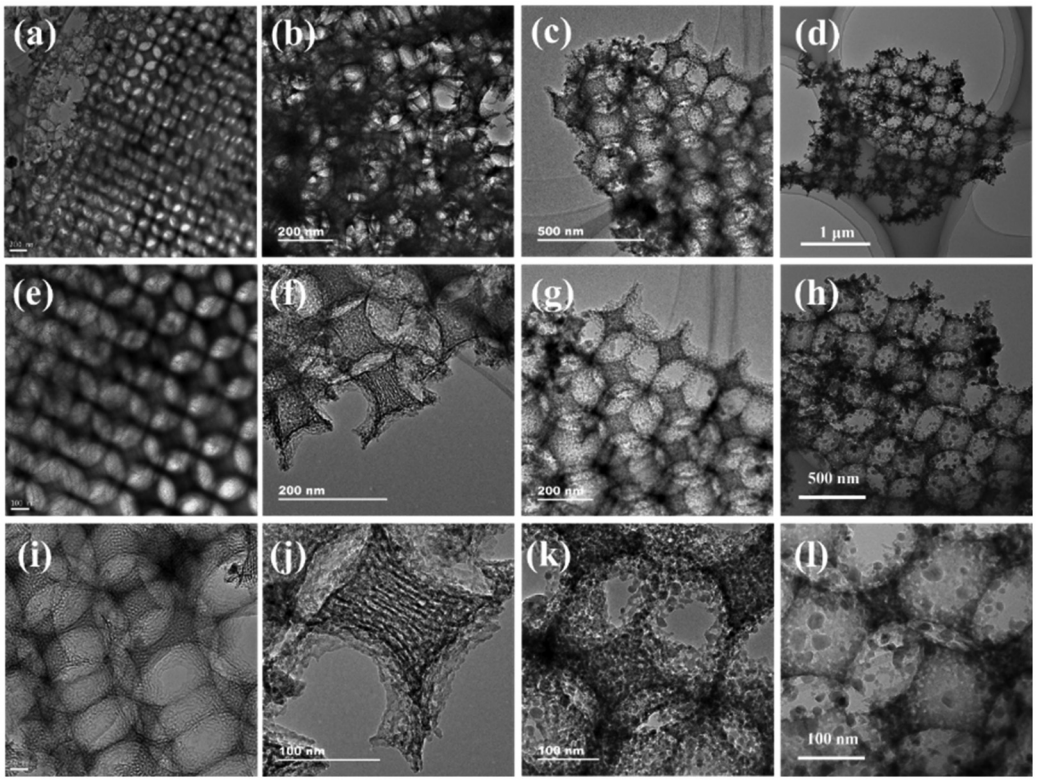

Fig. 5 TEM images of Al_2O_3 (a, e, i), $FeCrAlO_x$ (b, f, j), $FeVAlO_x$ (c, g, k), and $FeVCrAlO_x$ (d, h, l).

(Fig. 5l). This might be due to the generation of new crystal phases caused by the introduction of elements. And the lattice distortion might be caused by the formation of new crystal phases. Then the pore structure would deform or reorganize. The transition from ordered structure to disordered structure might indicate the successful introduction of V and Cr.

The change in crystal structure after the introduction of elements was studied by XRD. The results were shown in Fig. 6 and Fig. S5.† The $FeAlO_3$ (PDF#30-0024) was found in the XRD curves of $FeCrAlO_x$, $FeVAlO_x$, and $FeVCrAlO_x$ samples. The XRD curves of $FeVAlO_x$ and $FeCrAlO_x$ (Fig. 6a and b) showed that the V element exists as VO_x when V was introduced into the Fe-based catalysts. This might indicate that the Fe in the lattice

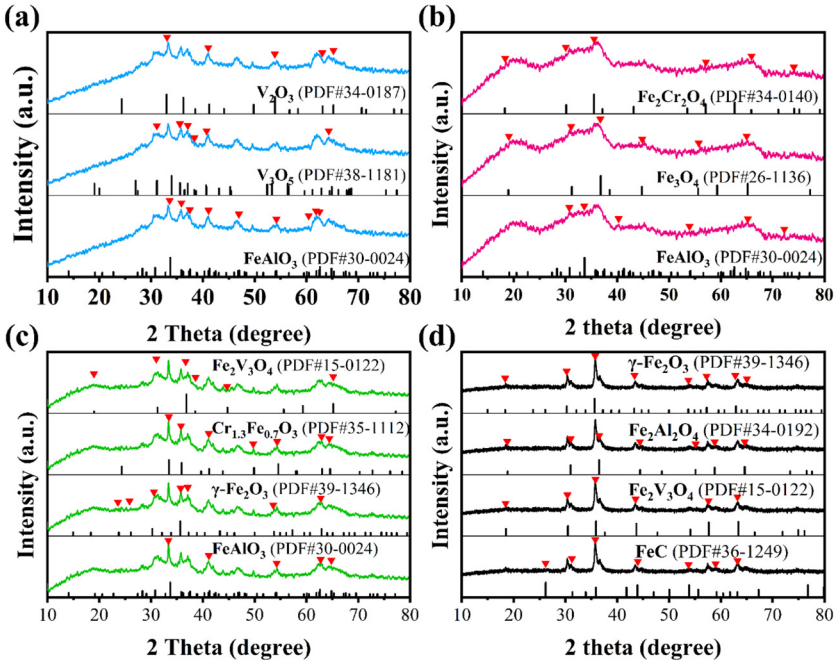

Fig. 6 XRD patterns of the $FeVAlO_x$ (a), $FeCrAlO_x$ (b), $FeVCrAlO_x$ (c), and used-$FeVCrAlO_x$ samples (d).

could not be replaced when only the V element was introduced. However, when Cr was introduced into iron-based catalysts, $Cr_{1.3}Fe_{0.7}O_3$ (PDF#35-1112) appears in the XRD curve of $FeCrAlO_x$ (Fig. 6b). This indicated that Fe in the lattice could be replaced by Cr. Finally, when V and Cr were introduced into the Fe-based catalyst together, the 2θ peaks at 33.44°, 35.79°, 41.17°, 49.72°, 54.35°, 62.90°, were considered as (104), (110), (113), (024), (116), (214) lattice planes of $Cr_{1.3}Fe_{0.7}O_3$ (PDF#35-1112). And the 2θ peaks at 18.96°, 31.01°, 36.67°, 38.59°, 44.68°, and 65.16°, were considered as (111), (220), (311), (222), (400), and (531) lattice planes of $Fe_2V_3O_4$ (PDF#15-0122). This indicated that V and Cr elements were successfully introduced into the Fe phase, and Cr might play an assistant role in the introduction of V. It's worth noting that, the appearance of 2θ peaks at 23.66°, 25.99°, 37.17°, 62.83°, 64.97°, were considered as (210), (211), (222), (440), (530) lattice planes of γ-Fe_2O_3 (PDF#39-1346). This indicated that the highly active γ-Fe_2O_3 phase was formed after the introduction of V and Cr. It could be found that the introduction of V and Cr changed the crystal structure of the catalyst and promoted the formation of γ-Fe_2O_3. This was beneficial to improving the mobility of lattice oxygen and the catalytic activity. This also elucidated the reason for the good catalytic activity of the catalyst. It should be emphasized that there is a clear difference between the catalyst before and after the reaction. As shown in Fig. S6,† the surface of the used catalyst was coated with a dark-colored substance, which potentially corresponds to catalyst deactivation. According to carbon balance (Fig. S7†), it could be found that the amount of carbon decreased after the reaction. This might be because carbon species. To better understand the catalyst changes before and after the reaction. XRD was performed on the samples. As shown in Fig. 6d, the peaks at 35.78°, 43.98°, 59.01°, and 63.25°, were considered as (010), (111), (104), (212) lattice planes of FeC (PDF#03-0400), and 18.78°, 31.01°, 36.51°, 44.39°, 64.62°, were considered as (111), (220), (311), (400), (440) lattice planes of $Fe_2Al_2O_4$ (PDF#34-0192). This indicated that the crystalline phase changed after the reaction and the FeC phase was generated. And FeC might be due to deep dehydrogenation of olefins. Besides, Fig. S8† showed the XRD and the surface of the regenerated catalyst, and there was no obvious coke on the surface of catalyst (Fig. S8b†). However, compared to the fresh sample

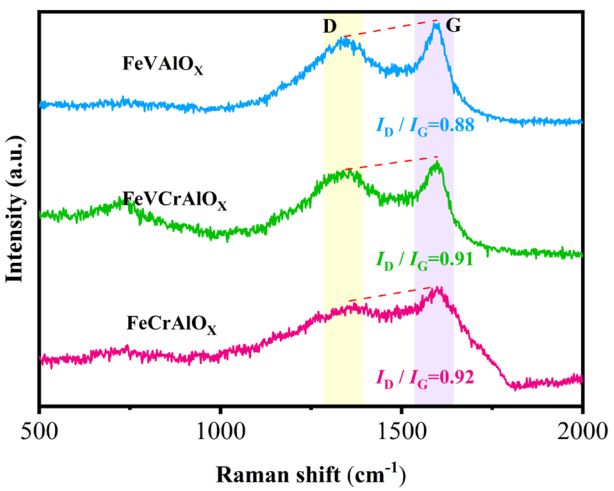

Fig. 7 Raman spectra of the used $FeVAlO_x$, $FeCrAlO_x$, and $FeVCrAlO_x$ samples.

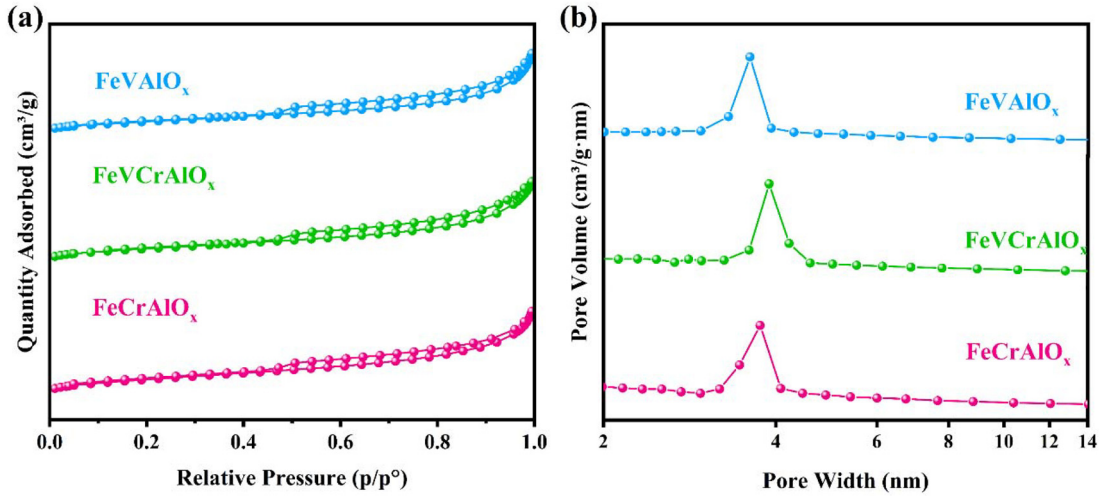

Fig. 8 Nitrogen adsorption–desorption isotherms (a) and pore size distribution (b) of FeVAlO$_x$, FeCrAlO$_x$, and FeVCrAlO$_x$ samples.

(Fig. S8a†), the regenerated catalyst had a significant decrease in the intensity of the peaks and the shape of the peaks was changed. This suggested the structure of the catalyst might change. Consequently, it can be inferred that the change in crystalline phase and coke formation were the main factors for catalyst deactivation and this make it difficult to restore its initial activity.

3.4. Study of coke formation

To visually show the type of carbon deposition, the used catalysts were analyzed by Raman spectroscopy. The D and G bands in the Raman spectra of the used catalysts indicated the presence of amorphous carbon deposition and graphitic carbon deposition, respectively.[29,30] According to the Tuinstra–Koenig law, the graphite crystallinity of the carbon deposition is inversely related to the integrated ratio of the D and G bands (I_D/I_G).[31,32] In Fig. 7, compared with FeCrAlO$_x$ (I_D/I_G = 0.92), the graphite crystallinity of the V introduced catalyst FeVAlO$_x$ (I_D/I_G = 0.88) was lower. Moreover, compared with FeCrAlO$_x$, the degree of graphitization of the catalyst FeVCrAlO$_x$ (I_D/I_G = 0.91) was also reduced. This suggested that the introduction of V was beneficial to inhibit the graphitizing of carbon deposits. And the lower degree of graphitization means that coke might be eliminated easily, this was consistent with O_2-TPO results of the used catalysts (Fig. S9†).[33,34] Compared with the FeCrAlO$_x$ catalysts, the FeVAlO$_x$ catalysts had smaller oxidation peaks and required less time for complete oxidation. This suggested that the coke on the FeVAlO$_x$ catalyst was less and it was easier to remove. When V was introduced, the catalyst FeVCrAlO$_x$ showed the similar results. This indicated that the catalysts with the introduction of V had better coking resistance.

The surface area, pore volume, and pore size of the FeVAlO$_x$, FeCrAlO$_x$, and FeVCrAlO$_x$ catalysts were tested by BET and the results were shown in Fig. 8 and Table 1. All the catalysts showed type IV isotherms with an H1 hysteresis loop, which indicated that the samples had abundant mesoporous

Table 1 BET result of synthesized FeVAlO$_x$, FeCrAlO$_x$, and FeVCrAlO$_x$ catalysts

Samples	Surface area ($m^2\ g^{-1}$)	Pore size (nm)	Pore volume ($cm^3\ g^{-1}$)
FeVAlO$_x$	64.04	7.80	0.166
FeCrAlO$_x$	92.32	6.78	0.178
FeVCrAlO$_x$	84.91	7.01	0.182

structures.[35–37] This is consistent with the results of TEM. Table 1 showed the specific surface area in the descending order: FeCrAlO$_x$ > FeVCrAlO$_x$ > FeVAlO$_x$. Compared with FeCrAlO$_x$, FeVCrAlO$_x$, and FeVAlO$_x$, it was found that the introduction of V resulted in a smaller specific surface area of the catalyst. According to the TEM analysis, the introduction of V destroyed the ordered mesoporous structure, which might be the reason for the reduction of specific surface area. In addition, it could be found that the pore volumes were in the following order: FeVCrAlO$_x$ > FeCrAlO$_x$ > FeVAlO$_x$. The large pore volume was beneficial in reducing the accumulation of reactants on the catalyst surface, which reduced the possibility of carbon deposition and coking. Owing to the large pore volume of FeVCrAlO$_x$ (0.182 $cm^3\ g^{-1}$), the catalyst exhibited good catalytic activity with the low coke formation.[38,39] Pore size followed the order: FeVAlO$_x$ > FeVCrAlO$_x$ > FeCrAlO$_x$. The comparison among FeVAlO$_x$, FeCrAlO$_x$, and FeVCrAlO$_x$ showed that the catalyst had the smallest pore size after the introduction of Cr (6.78 nm), the pore size became larger after the introduction of V (7.80 nm), and FeVCrAlO$_x$ had moderate pore sizes (7.01 nm) when both V and Cr were introduced. This might indicate that the pore size of the catalyst could be adjusted by the introduction of V. And the large pore size would facilitate the flow and diffusion of molecules, thereby reducing the coke formation.[40] This is consistent with the Raman results.

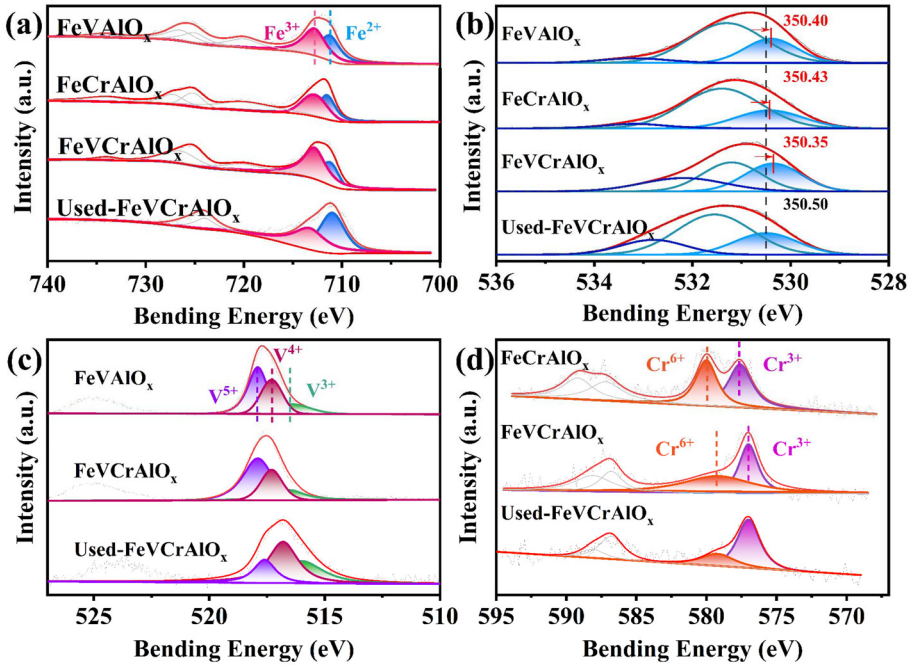

Fig. 9 XPS spectra of the (a) Fe 2p, (b) O 1s, (c) V 2p, (d) Cr 2p, on FeVAlO$_x$, FeCrAlO$_x$, FeVCrAlO$_x$, and used-FeVCrAlO$_x$.

3.5. Surface chemical environment and oxygen species analysis

The XPS test was used to study the valence of elements and their relative contents in samples. The results are shown in Fig. 9 and Table 2. As shown in Fig. 9a, the Fe 2p$_{3/2}$ peaks at 711.2 and 712.8 eV, could be regarded as Fe^{2+} and Fe^{3+} species.[41–43] The Fe^{3+} is considered as the active component in the oxidative dehydrogenation process and the oxidative dehydrogenation reaction was carried out through the Fe^{3+}/Fe^{2+} redox cycle. According to the data in Table 2, the percentage of Fe^{3+} was 50–60% when only V or Cr was introduced (FeVAlO$_x$ or FeCrAlO$_x$). However, when both components were added, the percentage of Fe^{3+} increased to 73.23% for FeVCrAlO$_x$. According to XRD analysis, the Fe_2O_3 phase appeared after the introduction of multi-component. This might be the reason for the increase in the percentage of Fe^{3+}. This suggested that multi-component catalysts have a higher oxidative dehydrogenation activity. In addition, the used catalysts were also analyzed to study the percentage of Fe^{3+}. The results showed that there was a decrease in the percentage of Fe^{3+} from 73.23% to 46.27% after the reaction. This indicated that Fe^{3+} played a key role in the reaction, its main function was to act as an efficient active component and facilitate the reaction process.

Then, the lattice oxygen content of different catalysts was analyzed. As shown in Fig. 9b, the O 1s peaks at about 530.4, 531.5, and 533 eV, were considered as the lattice oxygen (O_α), the surface adsorbed oxygen (O_β), and adsorbed water or hydroxyl molecules (O_γ) respectively.[44,45] It was noteworthy that the lattice oxygen binding energy of the sample (FeVCrAlO$_x$) was shifted towards lower values. This transition might be attributed to the inherent radius and charge density differences of vanadium (V), chromium (Cr), and iron (Fe). After the introduction of V and Cr, the lattice structure was modified. This led to the change in the local environment around the lattice oxygen, as a result, the strength of the metal–oxygen bond was weakened. The latter would enhance lattice oxygen mobility.[46] Moreover, the high proportion of O_α in the catalyst (FeVCrAlO$_x$), confirming the synergistic effect of V and Cr improved the mobility of lattice oxygen. The O_2-TPD was used to study the surface oxygen species (Fig. 10 and Table 3). Peaks below 400 °C were attributed to the adsorbed oxygen species. Peaks between 400 and 600 °C were considered as the surface lattice oxygen species. And peaks above 600 °C were regarded as the lattice oxygen species.[47–49] As shown in Fig. 10a, FeVCrAlO$_x$ showed the highest percentage of surface lattice oxygen species (54.75%). Then, by adjusting the amount of V and Cr introduced, the effect of element introduction on oxygen species was studied. With the introduction of Cr, the

Table 2 XPS data of FeVAlO$_x$, FeCrAlO$_x$, FeVCrAlO$_x$, and used-FeVCrAlO$_x$ catalysts

Samples	Fe^{3+}/Fe^{n+} [a] (%)	Cr^{6+}/Cr^{n+} [a] (%)	V^{5+}/V^{n+} [a] (%)	O_α/O_n [a] (%)
FeVAlO$_x$	54.20		47.77	26.97
FeCrAlO$_x$	50.46	48.72		25.67
FeVCrAlO$_x$	73.23	56.85	55.23	36.10
Used-FeVCrAlO$_x$	46.27	27.11	18.43	24.94

[a] The percentage of surface elements valences ($Fe^{n+} = Fe^{3+} + Fe^{2+}$), ($Cr^{n+} = Cr^{6+} + Cr^{3+}$), ($V^{n+} = V^{5+} + V^{4+} + V^{3+}$), and ($O_n = O_\alpha + O_\beta + O_\gamma$) were determined by XPS fitting analysis.

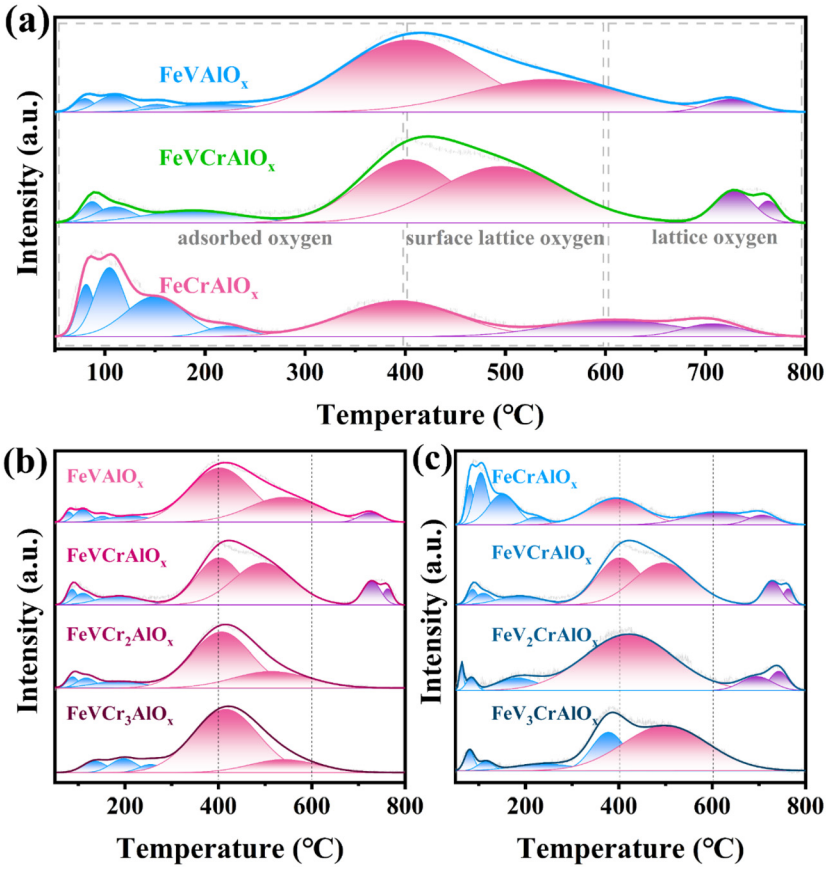

Fig. 10 O_2-TPD curves of the $FeVAlO_x$, $FeCrAlO_x$, $FeVCrAlO_x$ (a), and the curves of catalysts with different Cr (a) and V (b) contents.

Table 3 The percentage of oxygen species by O_2-TPD

Samples	Adsorbed oxygen (%)	Surface lattice oxygen (%)	Lattice oxygen (%)
$FeVAlO_x$	38.66	51.24	10.10
$FeVCrAlO_x$	33.26	54.75	11.99
$FeVCr_2AlO_x$	42.82	53.82	3.36
$FeVCr_3AlO_x$	43.72	52.90	3.38
$FeCrAlO_x$	62.56	22.19	15.26
$FeVCrAlO_x$	33.26	54.75	11.99
FeV_2CrAlO_x	42.75	42.73	14.53
FeV_3CrAlO_x	37.63	53.57	8.80

lattice oxygen percentage decreased and the surface lattice oxygen percentage increased. While with the introduction of V, the adsorbed oxygen percentage decreased and the surface lattice oxygen percentage increased Under the synergistic effect of V and Cr, the $FeVCrAlO_x$ sample had more surface lattice oxygen. This might indicate that V, Cr destroyed the original lattice structure. After the introduction of V and Cr, more lattice oxygen was activated and oxygen mobility was increased.

Besides, the V $2p_{3/2}$ peaks at 516.5, 517.3, and 517.9 eV in Fig. 9c were considered as V^{3+}, V^{4+}, and V^{5+} species, respectively.[50,51] From the Table 2, it could be found that compared with $FeVAlO_x$ (47.77%), $FeVCrAlO_x$ (55.23%) contained more V^{5+} species. This suggested that the introduction of multi-components brought more V^{5+} species. The analysis of the Used-$FeVCrAlO_x$ showed that the percentage of V^{5+} species was reduced to 18.43%. It demonstrated that V^{5+} might act as an active phase and participate in the reaction. Cr 2p spectrum was also studied. As shown in Fig. 9d, the peaks at 577 and 579 eV in Cr $2p_{3/2}$ were considered as Cr^{3+} and Cr^{6+} species.[52–55] It could be found that the binding energy of Cr is shifted to low binding energy after the introduction of the V. This might be due to the change in crystal structure after the introduction of V. This led to a change in the electron density around Cr and a decrease in binding energy. Similar to the V species, the Cr^{6+} species percentage increased from 48.72% to 56.85% when multi-components were introduced. And the percentage of Cr^{6+} species decreased to 27.11% after the reaction. The result indicated that Cr^{6+} species were also potential active phases in the reaction. Overall, the introduction of V and Cr not only increased the percentage of Fe^{3+} but also improved the lattice oxygen mobility. Besides, V and Cr were active components in the reaction. Under the synergistic effect, the multi-component catalyst activity was significantly enhanced.

3.6. Reduction ability and acid/base properties

H_2-TPR was used to study the effect of elemental introduction on catalyst activity (Fig. S10 and Table S3†). In Fig. S10,† the

peaks between 400–500 °C were attributed to the transition from Fe_2O_3 to Fe_3O_4, while the peaks between 600–700 °C were attributed to the transition from Fe_3O_4 to FeO.[56,57] Compared with the peak position of the samples ($FeVAlO_x$, $FeCrAlO_x$, and $FeVCrAlO_x$), the result showed that the addition of Cr led to a shift of the peak towards lower temperatures (from 467 to 464 °C). In order to clarify the influence of Cr and V on the reducibility. The relationship between the different contents of the elements and the reducibility of the catalyst was studied. the results were shown in Fig. S10b and c.† It could be found that the introduction of Cr led to a shift of the peaks toward lower temperatures (from 467 to 445 °C). This demonstrated that doping with Cr was beneficial for improving the reducibility of the catalyst. With the introduction of V, the peak shifted to the high temperatures (from 415 to 558 °C), this indicated that with the introduction of V, the catalyst became difficult to reduce. It is possible that the introduction of V changed the crystal structure. The vanadium species on the crystal surface changed from oligomeric vanadium oxide species to polymeric vanadium oxide species. While there are differences in the reducibility of different vanadium species, this leads to an increase in the reduction temperature.[58]

CO_2-TPD was used to study the basicity of the samples (Fig. S11†) and the results of the test by CO_2-TPD were shown in Table 4. As shown in Fig. S11a,† Peaks below 200 °C were considered as the weak basic sites, peaks between 200 and 350 °C were considered as the medium-strong basic sites, and peaks between 350 and 800 °C were considered as the strong basic sites.[59,60] Compared with $FeCrAlO_x$, $FeVAlO_x$, and $FeVCrAlO_x$ samples (Fig. S11b and c†), it was discovered that $FeVCrAlO_x$ had the greatest amount of strong basic sites (86.06%), followed by $FeVAlO_x$ (76.91%) and $FeCrAlO_x$ (63.39%). This suggested that the introduction of multi-component could effectively improve the strong basic sites. Besides, with the introduction of Cr, the strong basic sites decreased from 86.06% to 76.55% and then to 82.13%. When V was introduced, the percentage of strong basic sites decreased from 86.06% to 69.31%. This indicated that the multi-component had more strong base sites, and the introduction of excessive V or Cr would lead to a decrease in the strong base sites. This would be beneficial for the CO_2 utilization.[61]

Table 4 The percentage of base sites by CO_2-TPD

Samples	Weak basicity (%)	Medium basicity (%)	Strong basicity (%)
$FeVAlO_x$	7.81	15.28	76.91
$FeVCrAlO_x$	6.98	6.97	86.06
$FeVCr_2AlO_x$	9.02	14.43	76.55
$FeVCr_3AlO_x$	5.13	12.73	82.13
$FeCrAlO_x$	16.17	20.44	63.39
$FeVCrAlO_x$	6.98	6.97	86.06
FeV_2CrAlO_x	13.41	17.22	69.37
FeV_3CrAlO_x	10.62	20.07	69.31

In oxidative dehydrogenation reactions, acidic sites were found to play a crucial role by facilitating the breaking of C–C, C–H, and C–O bonds.[62] NH_3-TPD was used to study the acidity of the samples (Fig. S12†). Peaks below 300 °C were attributed to weak acid sites and peaks between 300 and 500 °C were considered as medium-strong acid sites.[63–65] Typically, weakly acidic sites provided a suitable environment for adsorption and activation. Strongly acidic sites promoted the reaction rate, while overly acidic sites resulted in reduced selectivity for the target product.[66–69] The respective effects of V and Cr were analyzed, and the results showed that the addition of Cr modified the weak and medium strong acidic sites (Fig. S12b†). While the introduction of V decreased the weak acid sites and increased the medium-strong acid sites (Fig. S12c†). Compared with the $FeVAlO_x$, $FeCrAlO_x$, and $FeVCrAlO_x$ samples (Fig. S12a†), it could be found that the multi-component catalyst $FeVCrAlO_x$ contained more medium strong acid sites. This suggested that the introduction of multicomponent catalysts could increase the medium-strong acid sites. And the suitable ratio of weak and strong acid sites promoted the dehydrogenation reaction.[70]

3.7. Catalytic performance in the presence of water

In order to study the effect of water on catalytic activity, the performance of the $FeVCrAlO_x$ samples was studied under different volume fractions of water (Fig. 11). The volume fraction was recorded as 0 when water was absent in the reaction. It was discovered that when the volume fraction of water rose, the BD yield increased first and then decreased (Fig. 11a). Compared with the yield in the absence of water (27.5%), the yield reached 33.1%, when the water volume fraction was 2.25% (Fig. 11b). Besides, the selectivity of BD increased from 31.2% to 38.9% (Fig. 11c), and the conversion of CO_2 increased from 15.7% to 19.3% (Fig. 11d). This demonstrated that the BD yield, BD selectivity, and the CO_2 conversion could be improved by a proper volume fraction of water. However, the conversion of 1-butene decreased after the addition of water. This might be due to the competitive adsorption of water with 1-butene on the surface of the catalyst, therefore the conversion of 1-butene was reduced.[71,72]

The catalytic activity of $FeVAlO_x$ and $FeCrAlO_x$ was studied at different water volume fractions (Fig. S13 and S14†). Fig. S15† showed the reaction orders of $FeVAlO_x$, $FeCrAlO_x$, and $FeVCrAlO_x$, for 1-butene consumption in the presence of water. The data Revealed the sensitivity to the presence of water differed among the different catalysts. The $FeCrAlO_x$ catalyst had a reaction order of 0.12, this indicated a relatively low sensitivity to water. The $FeVAlO_x$ catalyst had a reaction order of 0.17, suggesting it was more sensitive to the presence of water than the $FeCrAlO_x$. On the other hand, the multicomponent catalyst ($FeVCrAlO_x$) had a reactivity order of only 0.03. This indicated much lower sensitivity to changes in water concentration. This might be due to the strong adsorption capacity of its porous structure, so the adsorption or activation of water molecules is not the rate-determining step.[73] In order to study how water promoted the CO_2-ODH catalytic process.

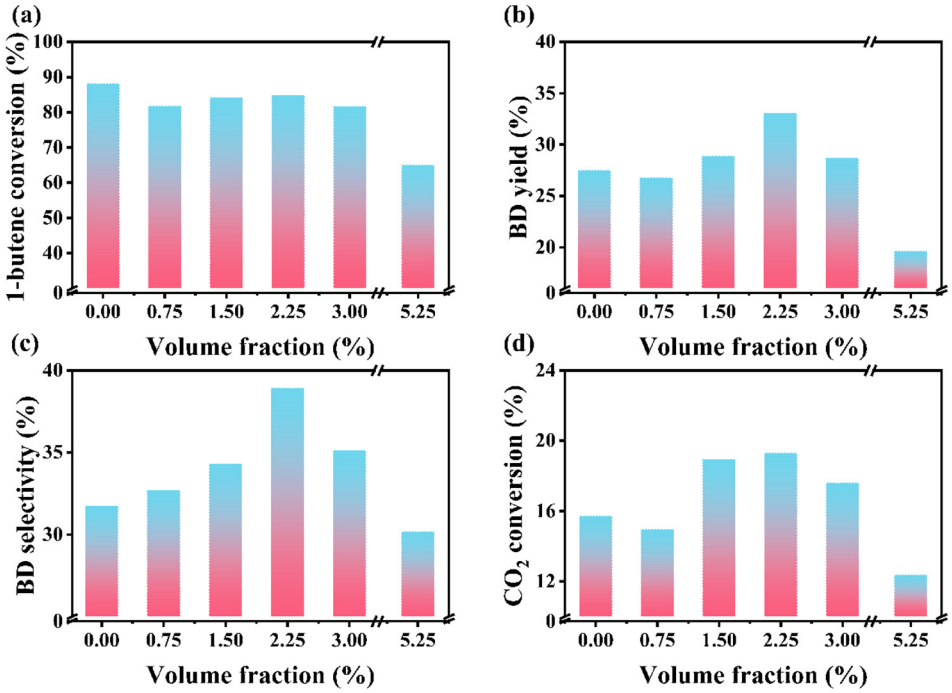

Fig. 11 Catalytic activity of FeVCrAlO$_x$ samples with different water volume fractions at 600 °C. (a) 1-Butene conversion. (b) BD yield, (c) BD selectivity, and (d) CO_2 conversion.

In situ DRIFTS was used to study the reaction in the absence/presence of water.

3.8. Reaction mechanism study

The *in situ* DRIFTS spectra of 1-butene adsorption at 100 °C were shown in Fig. 12. The peaks at 3088 cm^{-1} and 1651 cm^{-1} were regarded as the =CH$_2$ and the C=C stretching vibration of 1-butene.[74] This indicated that butene was effectively adsorbed on the catalyst surface over time. Fig. 13 showed the heating process at 110–350 °C with the introduction of CO_2. The peak at 2973 cm^{-1} could be regarded as the stretching vibration of the C–H bond of the CH_3 group[75] (Fig. 13c). The peaks at 1654 cm^{-1} and 1640 cm^{-1} were regarded as the C=C stretching vibration of 1-butene and 1,3-butadiene, respectively (Fig. 13b). As the temperature rose, the peak at 2973 cm^{-1} (–CH$_3$) decreased and then disappeared (the temperature is about 320 °C), which indicated that the terminal methyl group began to be consumed. And the peak at 1654 cm^{-1} gradually disappeared and the peak at 1640 cm^{-1} gradually appeared. This indicated that 1,3-butadiene was formed. The shift from 1654 to 1640 cm^{-1} might be due to the conjugation effect of 1,3-butadiene, then the C=C force constant was decreased and thus the C=C stretching vibrational phase was shifted towards the low-wave direction. This eventually leads to a red-shift. Similarly, the peaks at 3088 cm^{-1} and 3072 cm^{-1} (Fig. 13c) were regarded as the =CH$_2$ stretching vibrations of 1-butene and 1,3-butadiene[76,77] respectively. It could be found that as the temperature increased, the peaks at 3088 cm^{-1} gradually weakened and then disappeared, after that the peaks at 3072 cm^{-1} appeared and gradually became stronger. This might indicate that the =CH$_2$ of butene is consumed first and then disappeared during the conversion of 1-butene to 1,3-butadiene. Finally, the characteristic peak of 1,3-butadiene appeared. This might be that 1-butene was first converted into 2-butene and then the 2-butene was converted into 1,3-butadiene.[78]

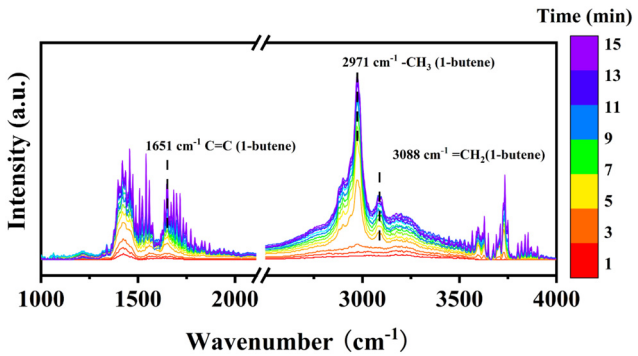

Fig. 12 *In situ* DRIFTS spectra of 1-butene adsorption at 100 °C over the FeVCrAlO$_x$ samples.

The reaction in the presence of water was also analyzed by *in situ* DRIFTS and the adsorption of butene at 100 °C was shown in Fig. S16.† The characteristic peaks at 3088 cm^{-1} and 1654 cm^{-1} were regarded as the =CH$_2$ and the C=C stretching vibration of 1-butene, and this indicated that 1-butene was effectively adsorbed on the catalyst surface over time. Fig. 14

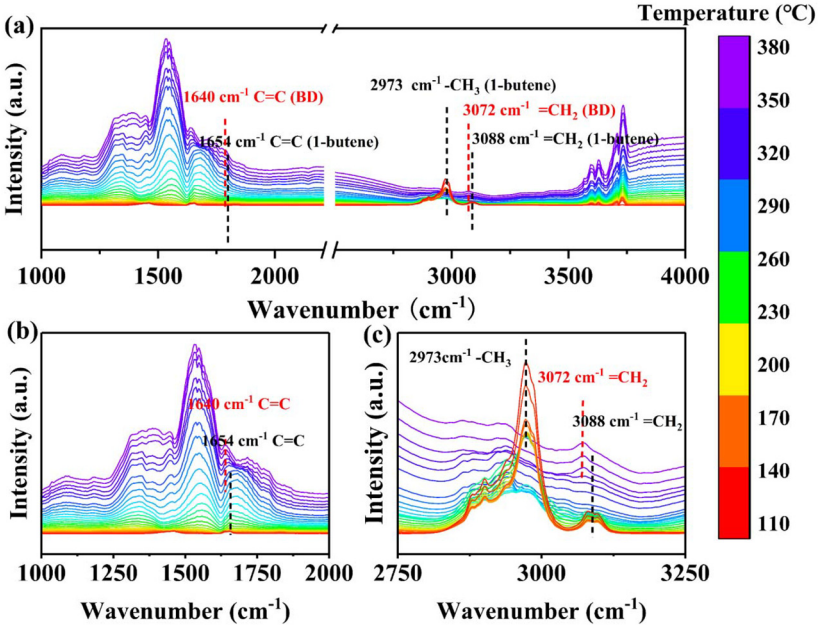

Fig. 13 *In situ* DRIFTS Spectra of FeVCrAlO$_x$ samples exposed to CO_2 and 1-butene steams.

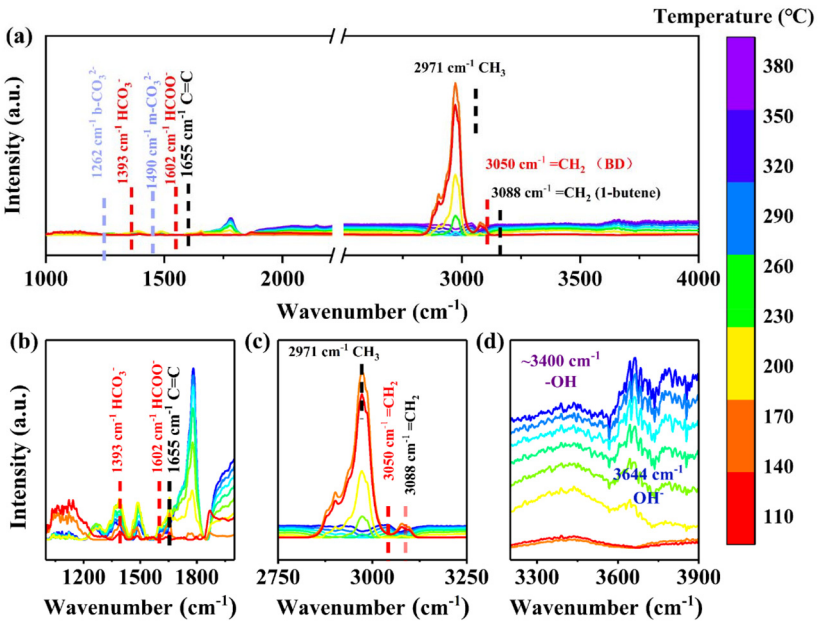

Fig. 14 *In situ* DRIFTS Spectra of FeVCrAlO$_x$ samples exposed to CO_2, 1-butene, and H_2O steams.

showed the variation of peaks from 110–380 °C in the presence of H_2O and CO_2. The peaks at 3088 cm^{-1} and 3050 cm^{-1} could be regarded as the $=CH_2$ stretching vibrations of 1-butene and 1,3-butadiene, respectively. The peak at 2971 cm^{-1} could be regarded as the stretching vibration of the C–H bond of the CH_3 group (Fig. 14c). After the addition of water and CO_2, it could be found that the terminal methyl group decreased rapidly and then disappeared (the temperature is about 290 °C), the peaks at 3088 cm^{-1} gradually weakened and then disappeared, and after that, the peaks at 3050 cm^{-1} gradually increased (Fig. 14c). This was similar to the change of peak in the absence of water. This indicated that 1,3-butadiene was produced. It is worth noting that when water was added, the peak of OH^- (3644 cm^{-1}), HCO_3^- (1393 cm^{-1}), and $HCOO^-$ (1602 cm^{-1}) appeared (Fig. 14b and d), and the hydroxyl peaks on the catalyst surface were enhanced (3400 cm^{-1}).[79–82] The reason might be that water was first cleaved to OH^- or surface hydroxyl groups by the catalyst, and the OH^- reacted with CO_2,

then the HCO_3^- was formed. As a result, the peak of surface hydroxyl groups and HCO_3^- increased. After that HCO_3^- + C_4H_8=C_4H_6 + $HCOO^-$ + H_2O might happen. This resulted in the peak appearing at 1602 cm^{-1} ($HCOO^-$). The characteristic peak of =CH_2 (BD) was located at 3050 cm^{-1}, rather than 3072 cm^{-1}, which might be due to the redshift caused by the $HCOO^-$. Finally, through the comparison of methyl peaks with and without water, it could be found that the methyl peaks decreased rapidly in the presence of water. It might be due to the improvement of CO_2 utilization in the presence of water. Thus, the reaction rate was accelerated, and the methyl peaks were rapidly consumed. In general, it could be found that the introduction of water not only improved the utilization of CO_2 but also changed the reaction path. This might be the reason for the increase in activity.

4. Conclusions

To study the synergetic effect of the introduction of multiple elements on the catalytic performance, a series of 3DOM Fe-based catalysts were prepared by the soft and hard templates method. The three-dimensionally ordered macro–mesoporous structures were studied by SEM and TEM images. The $FeVCrAlO_x$ catalyst showed a better catalytic performance. The 1-butene conversion of 88.3% and the BD yield of 27.5%, were reached. The synergetic effects of the V and Cr on the catalytic performances were studied respectively. The results showed that the introduction of Cr was beneficial for the conversion of CO_2, and the introduction of V was beneficial for the selectivity of BD. Moreover, when V and Cr were introduced together, the formation of γ-Fe_2O_3 was one of the reasons for the enhancement of catalytic activity. XPS and O_2-TPD studies showed that the introduction of multi-components improved the mobility of lattice oxygen. Compared with the $FeVAlO_x$ and $FeCrAlO_x$ samples, the $FeVCrAlO_x$ had surface lattice oxygen, and the proportion reached 36.10%. And the active components were also enriched (the proportion of Fe^{3+}, Cr^{6+}, and V^{5+} reached 73.23%, 56.85%, and 55.23%, respectively). This might be another reason for the improvement of catalytic activity. The XRD and Raman studies showed that the rapid deactivation of the catalyst was due to the coke formation, and the introduction of V was beneficial for the reduction of coke formation. In addition, by introducing water into the reaction process, the role of water in the catalytic process was clarified. The *in situ* DRIFTS tests showed that the addition of H_2O might enhance the utilization of CO_2 and change the reaction route. In the reaction process, water was cleaved to OH^- or surface hydroxyl groups. The OH^- reacted with CO_2. As a result of this, the HCO_3^- was formed. In this way, CO_2 participated in the reaction in the form of HCO_3^-. The catalytic activity was enhanced by the introduction of water. Finally, this study not only provides useful insights for the efficient utilization of CO_2 but also generates new ideas for the design of efficient dehydrogenation catalysts.

Data availability

The data supporting this article have been included as part of the ESI.†

Conflicts of interest

The authors declare no conflict of interest.

Acknowledgements

This work was supported by the Major Science and Technology Project of Gansu (23ZDFA016), Key Research and Development Program of Gansu Province, State Key Laboratory Program of the Lanzhou Institute of Chemical Physics, CAS (No. CHGZ-202213), LICP Cooperation Foundation for Young Scholars (HZJJ23-3) and West Light Foundation of Chinese Academy of Sciences (xbzg-zdsys-202318).

References

1 P. Tamizhdurai, V. L. Mangesh, A. A. A. Bahajjaj, U. Rajai, M. Govindasamy, R. Vasanthi, R. Kumaran and T. Augustine, Ionic liquid supported on mesoporous Pd/SBA-15 during the manufacture of 1,3-butadiene using ethanol at lower temperature reaction, *Fuel*, 2023, **345**, 128235.
2 L. Qi, Y. Zhang, M. Babucci, C. Chen, P. Lu, J. Li, C. Dun, A. S. Hoffman, J. J. Urban, M. Tsapatsis, S. R. Bare, Y. Han, B. C. Gates and A. T. Bell, Dehydrogenation of Propane and n-Butane Catalyzed by Isolated $PtZn_4$ Sites Supported on Self-Pillared Zeolite Pentasil Nanosheets, *ACS Catal.*, 2022, **12**, 11177–11189.
3 P. del Campo, M. T. Navarro, S. K. Shaikh, M. D. Khokhar, F. Aljumah, C. Martínez and A. Corma, Propene Production by Butene Cracking. Descriptors for Zeolite Catalysts, *ACS Catal.*, 2020, **10**, 11878–11891.
4 W. C. White, Butadiene production process overview, *Chem.-Biol. Interact.*, 2007, **166**, 10–14.
5 B. Yan, L. Wang, B. Wang, F. Alam, Z. Xiao, J. Li and T. Jiang, Constructing a high-efficiency iron-based catalyst for carbon dioxide oxidative dehydrogenation of 1-butene: The role of oxygen mobility and proposed reaction mechanism, *Appl. Catal., A*, 2019, **572**, 71–79.
6 K. Yang, J. Li, C. Wei, Z. Zhao and Z. Liu, Coupling Conversion of CO_2 and n-Butane Over Modified ZSM-5: Incorporation of the Carbon from CO_2 into Hydrocarbon Products, *ACS Catal.*, 2023, **13**, 10405–10417.
7 S. T. Rahman, J.-R. Choi, J.-H. Lee and S.-J. Park, The Role of CO_2 as a Mild Oxidant in Oxidation and Dehydrogenation over Catalysts: A Review, *Catalysts*, 2020, **10**, 1075.
8 X. Li, S. Wang, L. Li, X. Zu, Y. Sun and Y. Xie, Opportunity of Atomically Thin Two-Dimensional Catalysts for

Promoting CO_2 Electroreduction, *Acc. Chem. Res.*, 2020, **53**, 2964–2974.

9 Y. Dai, Y. Wu, H. Dai, X. Gao, S. Tian, J. Gu, X. Yi, A. Zheng and Y. Yang, Effect of coking and propylene adsorption on enhanced stability for Co^{2+}-catalyzed propane dehydrogenation, *J. Catal.*, 2021, **395**, 105–116.

10 X. Chen, M. Ge, Y. Li, Y. Liu, J. Wang and L. Zhang, Fabrication of highly dispersed Pt-based catalysts on γ-Al_2O_3 supported perovskite Nano islands: High durability and tolerance to coke deposition in propane dehydrogenation, *Appl. Surf. Sci.*, 2019, **490**, 611–621.

11 T. Zeng, G. Sun, C. Miao, G. Yan, Y. Ye, W. Yang and P. Sautet, Stabilizing Oxidative Dehydrogenation Active Sites at High Temperature with Steam: $ZnFe_2O_4$-Catalyzed Oxidative Dehydrogenation of 1-Butene to 1,3-Butadiene, *ACS Catal.*, 2020, **10**, 12888–12897.

12 X. Li, B. Yan, S. Yao, S. Kattel, J. G. Chen and T. Wang, Oxidative dehydrogenation and dry reforming of n-butane with CO_2 over NiFe bimetallic catalysts, *Appl. Catal., B*, 2018, **231**, 213–223.

13 X. Zhang, J. Li, W. Liu, Y. Zheng, J. An, W. Xin, Z. Liu, L. Xu, X. Li and X. Zhu, Synergistic Effect of Zinc and Iron in the CO_2-Assisted Oxidative Dehydrogenation of Propane, *ACS Catal.*, 2023, **13**, 14864–14873.

14 B. L. Yang, M. C. Kung and H. H. Kung, Reasons for the different selectivities in the selective oxidation of butene on α- and γ-Fe_2O_3, *J. Catal.*, 1984, **89**, 172–176.

15 H. Lee, J. C. Jung, H. Kim, Y.-M. Chung, T. J. Kim, S. J. Lee, S.-H. Oh, Y. S. Kim and I. K. Song, Effect of Divalent Metal Component (MeII) on the Catalytic Performance of $MeIIFe_2O_4$ Catalysts in the Oxidative Dehydrogenation of n-Butene to 1,3-Butadiene, *Catal. Lett.*, 2008, **124**, 364–368.

16 J. A. Toledo, P. Bosch, M. A. Valenzuela, A. Montoya and N. Nava, Oxidative dehydrogenation of 1-butene over Zn-Al ferrites, *J. Mol. Catal. A: Chem.*, 1997, **125**, 53–62.

17 M. Hye Jeong, D. Hyung Lee, J. Won Moon, J. Sun, J. Soon Choi, D. Sik Hong, C.-H. Chung and J. Wook Bae, Oxidative dehydrogenation of ethane and subsequent CO_2 activation on Ce-incorporated $FeTiO_x$ metal oxides, *Chem. Eng. J.*, 2022, **433**, 134621.

18 S. Zhang, C. Zhou, S. Wang, Z. Qin, G. Shu, C. Wang, L. Song, L. Zheng, X. Wei, K. Ma and H. Yue, Facilitating CO_2 dissociation via Fe doping on supported vanadium oxides for intensified oxidative dehydrogenation of propane, *Chem. Eng. J.*, 2024, **481**, 148231.

19 X. Zheng, B. Li, L. Shen, Y. Cao, Y. Zhan, S. Zheng, S. Wang and L. Jiang, Oxygen vacancies engineering of Fe doped $LaCoO_3$ perovskite catalysts for efficient H_2S selective oxidation, *Appl. Catal., B*, 2023, **329**, 122526.

20 N. Gao, Y. Zhou, M. Fan, H. Xu, Y. Chen and S. Shen, Promoting effect and role of alkaline earth metal added to ZrO_2-TiO_2-supported CeO_2 for dichloromethane oxidation, *Chem. Eng. J.*, 2020, **396**, 125193.

21 S. Yang, Z. Qi, Y. Wen, X. Wang, S. Zhang, W. Li and S. Li, Generation of abundant oxygen vacancies in Fe doped δ-MnO_2 by a facile interfacial synthesis strategy for highly efficient catalysis of VOCs oxidation, *Chem. Eng. J.*, 2023, **452**, 139657.

22 L. Song, H. Zhang, Z. Nie, J. Tian, Y. Liu, C. Ma, P. Liu, Q. Ren, J. Xiong, H. Huang, W. Yang, D. Cao, M. Fu and D. Ye, Ni Doping Promotes C–H Bond Activation and Conversion of Key Intermediates for Total Oxidation of Methane over Co_3O_4 Catalysts, *ACS Catal.*, 2023, **13**, 15779–15793.

23 Y.-L. Shan, Y.-A. Zhu, Z.-J. Sui, D. Chen and X.-G. Zhou, Insights into the effects of steam on propane dehydrogenation over a Pt/Al_2O_3 catalyst, *Catal. Sci. Technol.*, 2015, **5**, 3991–4000.

24 X. Zhao, T. Chen, Y. Wang, K. Li, R. Zhan and H. Lin, Effect of electric field and water on Pd-based catalyst for complete oxidation of methane: Study on promotion and deactivation, *Chem. Eng. J.*, 2023, **457**, 141126.

25 H. Tian, W. Li, L. He, Y. Zhong, S. Xu, H. Xiao and B. Xu, Rationalizing kinetic behaviors of isolated boron sites catalyzed oxidative dehydrogenation of propane, *Nat. Commun.*, 2023, **14**, 6520.

26 J. Long, S. Tian, S. Wei, H. Lin, G. Shi, X. Zong, Y. Yang, D. Yang, Y. Tang and Y. Dai, Direct dehydrogenation of propane over Co@silicalite-1 zeolite: Steaming-induced restructuring of Co^{2+} active sites, *Appl. Surf. Sci.*, 2023, **614**, 156238.

27 Z. Shi, F. Dong, Z. Tang and X. Dong, Design Sr, Mn-doped 3DOM $LaCoO_3$ perovskite catalysts with excellent SO_2 resistance for benzene catalytic combustion, *Chem. Eng. J.*, 2023, **473**, 145476.

28 W. Han, S. Wu, F. Dong, W. Han, Y. Chu, L. Su and Z. Tang, A confined growth strategy to construct 3DOM SiO_2 nanoreactor *in situ* embedded Co_3O_4 nanoparticles catalyst for the catalytic combustion of VOCs: Superior H_2O and SO_2 resistance, *Nano Res.*, 2024, **17**, 207–220.

29 S. Dong, P. Alvarez, N. Paterson, D. R. Dugwell and R. Kandiyoti, Study on the Effect of Heat Treatment and Gasification on the Carbon Structure of Coal Chars and Metallurgical Cokes using Fourier Transform Raman Spectroscopy, *Energy Fuels*, 2009, **23**, 1651–1661.

30 S. Weber, D. Batey, S. Cipiccia, M. Stehle, K. L. Abel, R. Glaser and T. L. Sheppard, Hard X-Ray Nanotomography for 3D Analysis of Coking in Nickel-Based Catalysts, *Angew. Chem., Int. Ed.*, 2021, **60**, 21772–21777.

31 J. Chen, Y. Liu, Z. Chen, J. Yue, Y. Tian, C. Zheng and J. Zhang, Highly Efficient Transformation of Tar Model Compounds into Hydrogen by a Ni–Co Alloy Nanocatalyst During Tar Steam Reforming, *Environ. Sci. Technol.*, 2024, **58**, 3540–3551.

32 S. A. Theofanidis, V. V. Galvita, H. Poelman, R. Batchu, L. C. Buelens, C. Detavernier and G. B. Marin, Mechanism of carbon deposits removal from supported Ni catalysts, *Appl. Catal., B*, 2018, **239**, 502–512.

33 Y. Liu, Y. Chen, Z. Gao, X. Zhang, L. Zhang, M. Wang, B. Chen, Y. Diao, Y. Li, D. Xiao, X. Wang, D. Ma and C. Shi, Embedding high loading and uniform Ni nanoparticles

into silicalite-1 zeolite for dry reforming of methane, *Appl. Catal., B*, 2022, **307**, 121202.

34 K. Cao, M. Gong, J. Yang, J. Cai, S. Chu, Z. Chen, B. Shan and R. Chen, Nickel catalyst with atomically-thin meshed cobalt coating for improved durability in dry reforming of methane, *J. Catal.*, 2019, **373**, 351–360.

35 P. A. Monson, Understanding adsorption/desorption hysteresis for fluids in mesoporous materials using simple molecular models and classical density functional theory, *Microporous Mesoporous Mater.*, 2012, **160**, 47–66.

36 B. Liu, J. Xiao, L. Xu, Y. Yao, B. F. O. Costa, V. F. Domingos, E. S. Ribeiro, F.-N. Shi, K. Zhou, J. Su, H. Wu, K. Zhong, J. A. Paixão and J. M. Gil, Gelatin-assisted sol–gel derived TiO_2 microspheres for hydrogen storage, *Int. J. Hydrogen Energy*, 2015, **40**, 4945–4950.

37 D. Tuncel and A. N. Ökte, Efficient photoactivity of TiO_2-hybrid-porous nanocomposite: Effect of humidity, *Appl. Surf. Sci.*, 2018, **458**, 546–554.

38 M. Ghazimoradi, S. Soltanali, N. Safari and H. Ghassabzadeh, Synthesis of fluorinated ZSM-5 catalysts: fluoride effect on structure properties and coke resistance in n-hexane catalytic cracking, *J. Mater. Sci.*, 2023, **58**, 11551–11567.

39 P. Sirous Rezaei, H. Shafaghat and W. M. A. W. Daud, Suppression of coke formation and enhancement of aromatic hydrocarbon production in catalytic fast pyrolysis of cellulose over different zeolites: effects of pore structure and acidity, *RSC Adv.*, 2015, **5**, 65408–65414.

40 M.-H. Sun, J. Zhou, Z.-Y. Hu, L.-H. Chen, L.-Y. Li, Y.-D. Wang, Z.-K. Xie, S. Turner, G. Van Tendeloo, T. Hasan and B.-L. Su, Hierarchical Zeolite Single-Crystal Reactor for Excellent Catalytic Efficiency, *Matter*, 2020, **3**, 1226–1245.

41 T. Yamashita and P. Hayes, Analysis of XPS spectra of Fe^{2+} and Fe^{3+} ions in oxide materials, *Appl. Surf. Sci.*, 2008, **254**, 2441–2449.

42 A. Rodriguez-Gomez, S. Ould-Chikh, J. Castells-Gil, A. Aguilar-Tapia, P. Bordet, M. A. Alrushaid, C. Marti-Gastaldo and J. Gascon, Fe-MOF Materials as Precursors for the Catalytic Dehydrogenation of Isobutane, *ACS Catal.*, 2022, **12**, 3832–3844.

43 Y.-n. Sun, L. Tao, T. You, C. Li and H. Shan, Effect of sulfation on the performance of Fe_2O_3/Al_2O_3 catalyst in catalytic dehydrogenation of propane to propylene, *Chem. Eng. J.*, 2014, **244**, 145–151.

44 Z. Wen, J. Ke, J. Xu, S. Guo, Y. Zhang and R. Chen, One-step facile hydrothermal synthesis of flowerlike Ce/Fe bimetallic oxides for efficient As(v) and Cr(vi) remediation: Performance and mechanism, *Chem. Eng. J.*, 2018, **343**, 416–426.

45 B. Yang, L. Liu, G. Zou, X. Luo, H. Zhu and S. Xu, The roles of $ZnFe_2O_4$ and α-Fe_2O_3 in the biphasic catalyst for the oxidative dehydrogenation of n-butene, *J. Catal.*, 2020, **381**, 70–77.

46 Y. Xu, J. Dhainaut, J.-P. Dacquin, A.-S. Mamede, M. Marinova, J.-F. Lamonier, H. Vezin, H. Zhang and S. Royer, $La_{1-x}(Sr, Na, K)_xMnO_3$ perovskites for HCHO oxidation: The role of oxygen species on the catalytic mechanism, *Appl. Catal., B*, 2021, **287**, 119955.

47 T. Zheng, W. Li, C. Li, S. An, Y. Jiang and L. Yuan, Single-step methane to methanol over lanthanum cerium oxide: The crucial role of surface reactive oxygen and carbonate species, *Mol. Catal.*, 2023, **551**, 113623.

48 S. Wu, H. Liu, Z. Huang, H. Xu and W. Shen, O-vacancy-rich porous MnO_2 nanosheets as highly efficient catalysts for propane catalytic oxidation, *Appl. Catal., B*, 2022, **312**, 121387.

49 W. Liu, S. Yang, H. Yu, S. Liu, H. Li, Z. Shen, Z. Song, X. Chen and X. Zhang, Boosting the total oxidation of toluene by regulating the reactivity of lattice oxygen species and the concentration of surface adsorbed oxygen, *Sep. Purif. Technol.*, 2023, **325**, 124597.

50 K. P. Thaba, M. M. Mphahlele-Makgwane, P. I. Kyesmen, M. Diale, P. G. L. Baker and P. R. Makgwane, Composition-dependent structure evolution of $FeVO_4$ nano-oxide and its visible-light photocatalytic activity for degradation of methylene blue, *Colloids Surf., A*, 2022, **633**, 127856.

51 T. Boningari, D. K. Pappas and P. G. Smirniotis, Metal oxide-confined interweaved titania nanotubes M/TNT (M = Mn, Cu, Ce, Fe, V, Cr, and Co) for the selective catalytic reduction of NO_x in the presence of excess oxygen, *J. Catal.*, 2018, **365**, 320–333.

52 S.-H. Zhang, M.-F. Wu, T.-T. Tang, Q.-J. Xing, C.-Q. Peng, F. Li, H. Liu, X.-B. Luo, J.-P. Zou, X.-B. Min and J.-M. Luo, Mechanism investigation of anoxic Cr(vi) removal by nano zero-valent iron based on XPS analysis in time scale, *Chem. Eng. J.*, 2018, **335**, 945–953.

53 Y. Qi, M. Jiang, Y.-L. Cui, L. Zhao and S. Liu, Novel reduction of Cr(vi) from wastewater using a naturally derived microcapsule loaded with rutin–Cr(iii) complex, *J. Hazard. Mater.*, 2015, **285**, 336–345.

54 H. Nguyen Tran, Comment on "simultaneous and efficient removal of Cr(vi) and methyl orange on LDHs decorated porous carbons", *Chem. Eng. J.*, 2019, **359**, 810–812.

55 H.-P. Chao, Y.-C. Wang and H. N. Tran, Removal of hexavalent chromium from groundwater by Mg/Al-layered double hydroxides using characteristics of *in situ* synthesis, *Environ. Pollut.*, 2018, **243**, 620–629.

56 M. N. Abu Tahari, F. Salleh, T. S. Tengku Saharuddin, N. Dzakaria, A. Samsuri, M. W. Mohamed Hisham and M. A. Yarmo, Influence of hydrogen and various carbon monoxide concentrations on reduction behavior of iron oxide at low temperature, *Int. J. Hydrogen Energy*, 2019, **44**, 20751–20759.

57 M. N. Abu Tahari, F. Salleh, T. S. Tengku Saharuddin, A. Samsuri, S. Samidin and M. A. Yarmo, Influence of hydrogen and carbon monoxide on reduction behavior of iron oxide at high temperature: Effect on reduction gas concentrations, *Int. J. Hydrogen Energy*, 2021, **46**, 24791–24805.

58 Y.-P. Tian, P. Bai, S.-M. Liu, X.-M. Liu and Z.-F. Yan, VO_x–K_2O/γ-Al_2O_3 catalyst for nonoxidative dehydrogenation of isobutane, *Fuel Process. Technol.*, 2016, **151**, 31–39.

59 R. Cao, X. Wang, P. Ning, Y. Xie, L. Wang, Y. Ma, X. Li, H. Zhang and J. Liu, Advantageous Role of N-doping on K@Al in COS/CS_2 Hydrolysis: Diminished Oxygen Mobility and Rich basic sites, *Fuel*, 2023, **337**, 126882.

60 S. B. Alreshaidan, A. A. Ibrahim, A. H. Fakeeha, A. M. Almutlaq, F. A. Ali and A. S. Al-Fatesh, Effect of Modified Alumina Support on the Performance of Ni-Based Catalysts for CO_2 Reforming of Methane, *Catalysts*, 2022, **12**, 1066.

61 Z. Zhang, X. Hu, Y. Wang, S. Hu, J. Xiang, C. Li, G. Chen, Q. Liu, T. Wei and D. Dong, Regulation the reaction intermediates in methanation reactions via modification of nickel catalysts with strong base, *Fuel*, 2019, **237**, 566–579.

62 A. T. Al-Qathmi, G. Tanimu, H. S. Alasiri, Z. S. Qureshi, M. M. Hossain and Z. O. Malaibari, Influence of Zn and Fe promoters on Ni-Bi/γ-Al_2O_3 catalyst for oxidative dehydrogenation of n-butane to butadiene, *Mol. Catal.*, 2023, **540**, 113067.

63 R. Zong, H. Li, W. Ding and H. Huang, Highly Dispersed Pd on Zeolite/Carbon Nanocomposites for Selective Hydrodeoxygenation of Biomass-Derived Molecules under Mild Conditions, *ACS Sustainable Chem. Eng.*, 2021, **9**, 9891–9902.

64 M. Wang, N. Shang, W. Gao, X. Cheng, S. Gao and C. Wang, Anchoring Co on CeO_2 nanoflower as an efficient catalyst for hydrogenolysis of 5-hydroxymethylfurfural, *Fuel*, 2023, **354**, 129433.

65 S. Wu, S. Wu, F. Dong, Y. Xi, P. Wang, Y. Chu, Z. Tang and J. Zhang, Elucidating the nature role of acid etching on the $CoMnO_x$ catalyst with outstanding performance for the catalytic combustion of o-dichlorobenzene, *Appl. Catal., B*, 2024, **342**, 123390.

66 Y. Chen, Y. Wang, Q. Ma, X. Gao and T.-S. Zhao, Cu modified VO_x/Silicalite-1 catalysts for propane dehydrogenation in CO_2 atmosphere, *Fuel*, 2024, **363**, 130819.

67 S. Rimaz, L. Chen, A. Monzón, S. Kawi and A. Borgna, Enhanced selectivity and stability of Pt-Ge/Al_2O_3 catalysts by Ca promotion in propane dehydrogenation, *Chem. Eng. J.*, 2021, **405**, 126656.

68 B. Liu, H. Zhao, J. Yang, J. Zhao, L. Yan, H. Song and L. Chou, Fabrication of hierarchically porous $MgFe_2O_4$/N-doped carbon composites for oxidative dehydrogenation of isobutane, *Appl. Surf. Sci.*, 2020, **531**, 147219.

69 C. Yu, H. Xu, Q. Ge and W. Li, Properties of the metallic phase of zinc-doped platinum catalysts for propane dehydrogenation, *J. Mol. Catal. A: Chem.*, 2007, **266**, 80–87.

70 S. Lawson, K. Baamran, K. Newport, T. Alghamadi, G. Jacobs, F. Rezaei and A. A. Rownaghi, Integrated direct air capture and oxidative dehydrogenation of propane with CO_2 at isothermal conditions, *Appl. Catal., B*, 2022, **303**, 120907.

71 G. Liu, H. Sun, H. Wang and Z. Qu, Rational tuning towards B-sites (B = Mn, Co, Al) on CoB_2O_4 binary oxide for efficient selective catalytic oxidation of ammonia, *Chem. Eng. J.*, 2023, **453**, 139941.

72 R. Gholami, M. Alyani and K. J. Smith, Deactivation of Pd Catalysts by Water during Low Temperature Methane Oxidation Relevant to Natural Gas Vehicle Converters, *Catalysts*, 2015, **5**, 561–594.

73 X. Zhang, J. Li, Y. Zheng, W. Xin, J. An, X. Zhu and X. Li, Structural reconstruction of iron oxide induces stable catalytic performance in the oxidative dehydrogenation of n-butane to 1,3-butadiene, *Chem. Eng. J.*, 2023, **473**, 145370.

74 Q. Zhu, G. Wang, H. Zhang, X. Zhu and C. Li, n-Butane dehydrogenation over Ni-Sn/SiO_2: Adsorption modes and reaction paths of n-butane and 1-butene, *Appl. Catal., A*, 2018, **566**, 113–120.

75 C. Hu, J. Sun, D. Kang, Q. Zhu and Y. Yang, Mechanistic insights into complete hydrogenation of 1,3-butadiene over Pt/SiO_2: effect of Pt dispersion and kinetic analysis, *Catal. Sci. Technol.*, 2017, **7**, 2717–2728.

76 E. Castillejos-López, G. Agostini, M. Di Michel, A. Iglesias-Juez and B. Bachiller-Baeza, Synergy of Contact between ZnO Surface Planes and PdZn Nanostructures: Morphology and Chemical Property Effects in the Intermetallic Sites for Selective 1,3-Butadiene Hydrogenation, *ACS Catal.*, 2016, **7**, 796–811.

77 C. Hu, J. Sun, Y. Yang, Q. Zhu and B. Yu, Reaction pathway for partial hydrogenation of 1,3-butadiene over Pt/SiO_2, *Catal. Sci. Technol.*, 2017, **7**, 5932–5943.

78 W. Han, F. Dong, W. Han, X. Huang and Z. Tang, Constructing mesoporous $FeAlO_x$ based catalysts through framework-confined strategy with superior performance for the oxidative dehydrogenation of 1-butene with CO_2, *Chem. Eng. J.*, 2023, **475**, 146432.

79 Z.-W. Wang, Q. Wan, Y.-Z. Shi, H. Wang, Y.-Y. Kang, S.-Y. Zhu, S. Lin and L. Wu, Selective photocatalytic reduction CO_2 to CH_4 on ultrathin TiO_2 nanosheet via coordination activation, *Appl. Catal., B*, 2021, **288**, 120000.

80 N. Liu, J. Wei, J. Xu, Y. Yu, J. Yu, Y. Han, K. Wang, J. I. Orege, Q. Ge and J. Sun, Elucidating the structural evolution of highly efficient Co–Fe bimetallic catalysts for the hydrogenation of CO_2 into olefins, *Appl. Catal., B*, 2023, **328**, 122476.

81 X. Li, H. Jiang, C. Ma, Z. Zhu, X. Song, X. Li, H. Wang, P. Huo and X. Chen, Construction of a multi-interfacial-electron transfer scheme for efficient CO_2 photoreduction: a case study using $CdIn_2S_4$ micro-flower spheres modified with Au nanoparticles and reduced graphene oxide, *J. Mater. Chem. A*, 2020, **8**, 18707–18714.

82 W. Yan, Y. Zhang and Y. Bi, Subnanometric Bismuth Clusters Confined in Pyrochlore-$Bi_2Sn_2O_7$ Enable Remarkable CO_2 Photoreduction, *Angew. Chem., Int. Ed.*, 2023, **63**, e202316459.